

In-Situ Measurements of Free-Standing, Ultra-Thin Film Cracking in Bending

E. Hintsala¹  · D. Kiener² · J. Jackson³ · W.W. Gerberich¹

Received: 22 October 2014 / Accepted: 28 June 2015 / Published online: 11 July 2015
© Society for Experimental Mechanics 2015

Abstract Metallic thin films are widely used and relied upon for various technologies. Direct measurements of fracture toughness are rare for metallic thin films and existing methods for obtaining these measurements often do not provide characterization of the cracking process for determination of crack growth mechanisms. To rectify this, we explore a new technique which utilizes doubly clamped, *in-situ* three-point bend testing of micro-scale and nano-scale specimens. This is done by *in-situ* scanning electron microscopy (SEM) and transmission electron microscopy (TEM) mechanical testing for specimens with thicknesses of 2500 nm (SEM), 500 nm (SEM) and 100 nm (TEM). For *in-situ* TEM, a novel notching method is employed using the converged electron beam which achieves a notch radius of approximately 5 nm. Additionally, we present supporting characterization using Electron Backscatter Diffraction (EBSD) for 2500 nm thick specimens as a demonstration of the potential of this technique for understanding local deformation. Analysis of the acquired data presents several issues that require addressing, and recommendations for future improvements are given.

Keywords Electron backscatter diffraction · Fracture testing · Electron microscopy · Steel · Nanomechanics

✉ E. Hintsala
hints009@umn.edu

¹ Department of Chemical Engineering and Materials Science, University of Minnesota, Amundson Hall, 421 Washington Avenue SE, Minneapolis, MN 55455, USA

² Department of Materials Physics, Montanuniversität Leoben, Leoben, Austria

³ Idaho National Laboratory, Idaho Falls, ID, USA

Introduction

Both free-standing and supported metallic thin films are utilized in a variety of applications including microelectromechanical devices [1, 2] and interconnects [3]. These undergo multiple failure mechanisms such as delamination [4], channel cracking [5, 6] and surface cracking which can be coupled with time-dependent damage from load cycling [7] and environmental degradation [8]. While multiple techniques and analyses exist for studying delamination or channel cracking of deposited thin films, direct measurements of fracture toughness values are relatively rare. Some fracture toughness measurements have been made for relatively brittle ceramics, graphene sheets or semiconductors as a function of length scale in the range of 10–10 μm [9–11]. For more ductile metals and intermetallics, recent efforts have been undertaken to measure microscale fracture toughness in NiAl [12] and debonding at the nanoscale for Cu/CuSiAl multilayers [13].

For thin ductile films, greater fracture resistance and more stable crack advance with decreasing film thickness B would generally be expected as this has been the size effect trend in other materials (“Smaller is tougher” [14]). However, fracture instabilities could result from the increase in yield strength and a possible decrease in plastic energy dissipation when B is reduced. The work per unit fracture area in thin materials is proportional to the volume of the plastic region ($\alpha B^2 a$) divided by the crack extension area (Ba), where a is the crack length and α is a constant relating the plastic zone size to a . This has been extensively studied both experimentally [15, 16] and theoretically [17, 18], as recently reported by Hosokawa et al. [19]. At nano-scale thicknesses, relatively small applied stress intensities for crack initiation and growth have been found for Au (0.45 MPa-m^{1/2}) and Al (0.515 MPa-m^{1/2}) [20]. These stress intensity values may reflect a plastic

tearing process rather than true fracture instability, therefore characterization of the cracking process is needed to properly assess failure.

The predominant existing techniques for studying fracture in thin metallic films include nanoindentation, bulge testing, *in-situ* straining holders and MEMS devices. Traditional thin film nanoindentation techniques cannot be applied to free-standing films [21]. For free-standing films, thin film bulge testing [20], MEMS devices [22], and *in-situ* straining holders for both transmission electron microscopy (TEM) and scanning electron microscopy (SEM) [19, 23] can be applied, but only straining holders allow detailed characterization of the cracking process. Though straining holders give high stability for imaging, they are limited in the extraction of mechanical data, as the load or stress is mostly unknown. A possibly better compromise is to use *in-situ* nanoindenters, which can provide both mechanical data and imaging [24]. However, a specialized testing geometry is needed to apply them to studying fracture properties. To this end, we have utilized a novel doubly clamped *in-situ* three-point bend test, as recently introduced by Jaya et al. [25–27], to explore fracture processes in ductile materials at the micro- and nanoscale. Samples were prepared for both *in-situ* SEM and TEM using Focused Ion Beam (FIB) milling to explore the range of applicability of this technique and the evaluation of possible size effects.

Experimental Procedure

Sample Preparation

All specimens were taken from a 20 % cold-rolled bar of Nitronic 50, an austenitic stainless steel (12.5 % Ni, 22 % Cr, 5 % Mn, 2.25 % Mo, 0.3%N, 0.06 % C). The number average grain size for this material was found to be $\sim 10 \mu\text{m}$ by EBSD. Lamellae of approximately $10 \mu\text{m}$ thickness were prepared using a combination of electrical discharge machining, mechanical polishing, and electro-polishing as described in [28]. A special holder was used to fix the lamella which was compatible with SEM, FIB and TEM. A multi-step FIB processes, outlined in Appendix A1, was used to produce bending beams of different sizes with a constant 4:2:1 (Length:width:thickness) aspect ratio with thicknesses of 2500 nm (for SEM), 500 nm (for SEM) and 100 nm (for TEM). Beyond this point, some differences in the approach were necessary for the specimens designed for *in-situ* TEM. Accurate thickness measurements were performed for the 2500 nm and 500 nm thickness specimens by tilting the lamella 90° to an upright position in the SEM, but for the 100 nm thickness specimens this method was found insufficient due to resolution limits of the SEM. Instead, the zero-loss peak was compared to the plasmon peak from electron

energy loss spectrums as commonly done for thickness mapping, estimating an average atomic number of 26 [29].

All specimens also possessed a pre-notch traversing half the length of the bending beam, which is the most critical part of the sample preparation. The minimum available FIB current of 10pA is capable of producing a notch approximately 200 nm in width due to resolution limits for a typical FIB. Consequently, for a 100 nm thick beam with an 800 nm span, the notch as fabricated by the FIB would have been about one fourth of the length of the beam, as also observed by Kumar et al. [30, 31]. To improve this for the 100 nm thick beams, a much sharper notch was produced by a novel method utilizing the fully converged TEM beam to locally sputter material, resulting in a notch radius of approximately 5 nm. This is proposed to represent a natural crack as discussed in Appendix A2.

Characterization and Testing

An example of a 100 nm thick bending beam being tested in the TEM is shown in Fig. 1, where the thickness B is into the page, a_0 is the prenotch length, L the span, and b is the ligament such that the total bending beam width $W=b+a$. It is duly noted that FIB preparation results in residual damage from Gallium implantation and is a concern here. However, rapidly varying contrast, typical for local lattice damage, was not significant compared to other materials FIB prepared for *in-situ* mechanical testing as in [32].

The FIB-fabricated 3-point bending beams were tested with two separate *in-situ* testing instruments, dedicated for

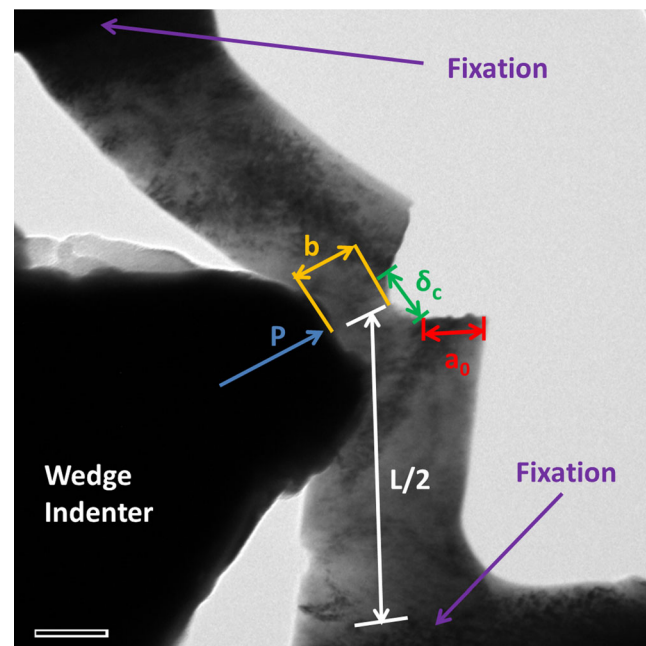


Fig. 1 Experimental setup during *in-situ* TEM loading, with important features and measurable quantities labeled where P is the applied load, $L/2$ is half the span, b is the ligament, a_0 is the initial crack length, and δ_c the crack tip opening displacement. Scale bar is 100 nm

use in the SEM and in the TEM, respectively. The *in-situ* SEM instrument utilized was an Asmec system inside of a Zeiss Leo 982 SEM. Imaging was performed using 10 keV accelerating voltage in the secondary electron mode. For the TEM experiments, a Hysitron PI-95 Picoindenter® holder was utilized *in-situ* in an image aberration-corrected JEOL 2100 F operating at 200 keV. For both instruments, testing was performed utilizing a wedge geometry tip (purchased from Synton-MDP, Nidau, CH) in displacement controlled mode, and for maximum bending, strain rates varied systematically from 0.0005 to 0.1 s^{-1} . Here, the maximum bending strain is defined as $6\delta b/L^2$, where δ is the indenter axis displacement. The strain rate variation was performed to account for possible strain-rate sensitivity [33], but had no apparent effect on the present results and will therefore not be discussed further. The wedge tip had a radius of curvature of $\sim 200 \text{ nm}$ for the SEM indenter system and $\sim 100 \text{ nm}$ for the TEM indenter system, respectively. The specimens were deformed using multiple (usually 4–6) loading cycles, which were typically about .05–0.1 bending strain in magnitude. Differences in approach distances and drift in the indenter system occurred, which were corrected by measuring the true indenter motion in the acquired video.

To explore characterization methods beyond imaging when utilizing electron microscopy, EBSD was utilized to track changes in grain size and crystal orientation with plastic deformation using a Zeiss LEO1525 operating at 30 keV and a step size of $0.10 \mu\text{m}$. It was found that only the 2500 nm thick specimens provided enough usable signal for EBSD evaluation. Additionally, since deformation and EBSD were performed in different instruments, some oxidation/contamination occurred, thereby reducing the quality of the EBSD data. Still, one high quality example of a 2500 nm beam was obtained and is shown in the results and discussion section. Orientation mapping techniques could also be extended into the TEM by using a scanning probe to gather diffraction data [34] for mapping local deformations during testing procedures.

Results and Discussion

2500 nm Beams

Figure 2 presents EBSD scans of a representative 2500 nm beam which underwent 5 load cycles, with cycle number increasing from top to bottom. Figure 2(a) shows grain orientations using the inverse pole figure (IPF) data, and Fig. 2(c) depicts the local misorientation relative to the grain average orientation. The load–displacement data for this 2500 nm beam tested *in-situ* in the SEM are presented in Fig. 2(b) with individual frames from the corresponding video at maximum deflection. As can be seen in Fig. 2(a), the plastic deformation

in the later stages of testing gives grain rotation in conjunction with the transition from elastic to plastic deformation in the load–displacement data. Large rotational changes appear to occur along the grain boundaries and are concentrated in the ligament region. For example, the tensile side just left of the notch begins with an orientation between the (001) and (111) axes and during loading rotates to an orientation between the (001) and (101) axis. A nearly perfectly opposite orientation change occurs just to the right of the notch on the compressive side, consistent with dislocation plasticity. There is a growing region of signal loss on the compressive side of the beam, which corresponds to a residual indenter impression. Additionally, the local misorientation shown in Fig. 2(c) exhibits significant changes. For example, the grain directly underneath the notch exhibits first a relaxation in local misorientation when the loading is predominantly elastic (Fig. 2(c) i–iii), while upon significant plastic deformation a strong misorientation localization is emerging right at the crack tip (Fig. 2(c) iv–v). Thus, the most significant changes in the EBSD data occur corresponding to the transition to fully plastic behavior in the load–displacement data, which is indicated by a flattening of the load versus displacement data. In the video frames presented in Fig. 2(b), the transition to plastic behavior is accompanied by a permanent retained opening of the crack. It should be noted when comparing Fig. 2(b, a & c) that the EBSD data is taken when the specimen is fully unloaded, so it is possible that reverse plasticity could occur during unloading. Additionally, cycle iv in Fig. 2 deviates from the rest of the tests due to slight indenter misalignment.

500 nm Beams

Figure 3 shows the load–displacement data for a representative 500 nm beam, with selected frames from the corresponding SEM video. The same highly ductile behavior is observed as in the 2500 nm beam, though the applied strains are much larger. The elastic region turns over to plastic as the plastic zones from the indenter tip and the crack tip overlap, creating a fully plastic hinge in the center of the beam which can support no increase in load. As plastic deformation proceeds, the crack tip continues to open, such that a critical crack condition is not achieved. However, the crack advances slightly through what appears to be a ductile tearing mode (Fig. 3 iii–v). The indenter was also still observed to leave a residual impression for specimens of this size.

100 nm beams

Figure 4 shows the load–displacement data for an exemplary 100 nm beam, with selected frames from the corresponding *in-situ* TEM video. Qualitatively, deformation appears to proceed similar to the larger specimen sizes, though some differences exist between the 100 nm

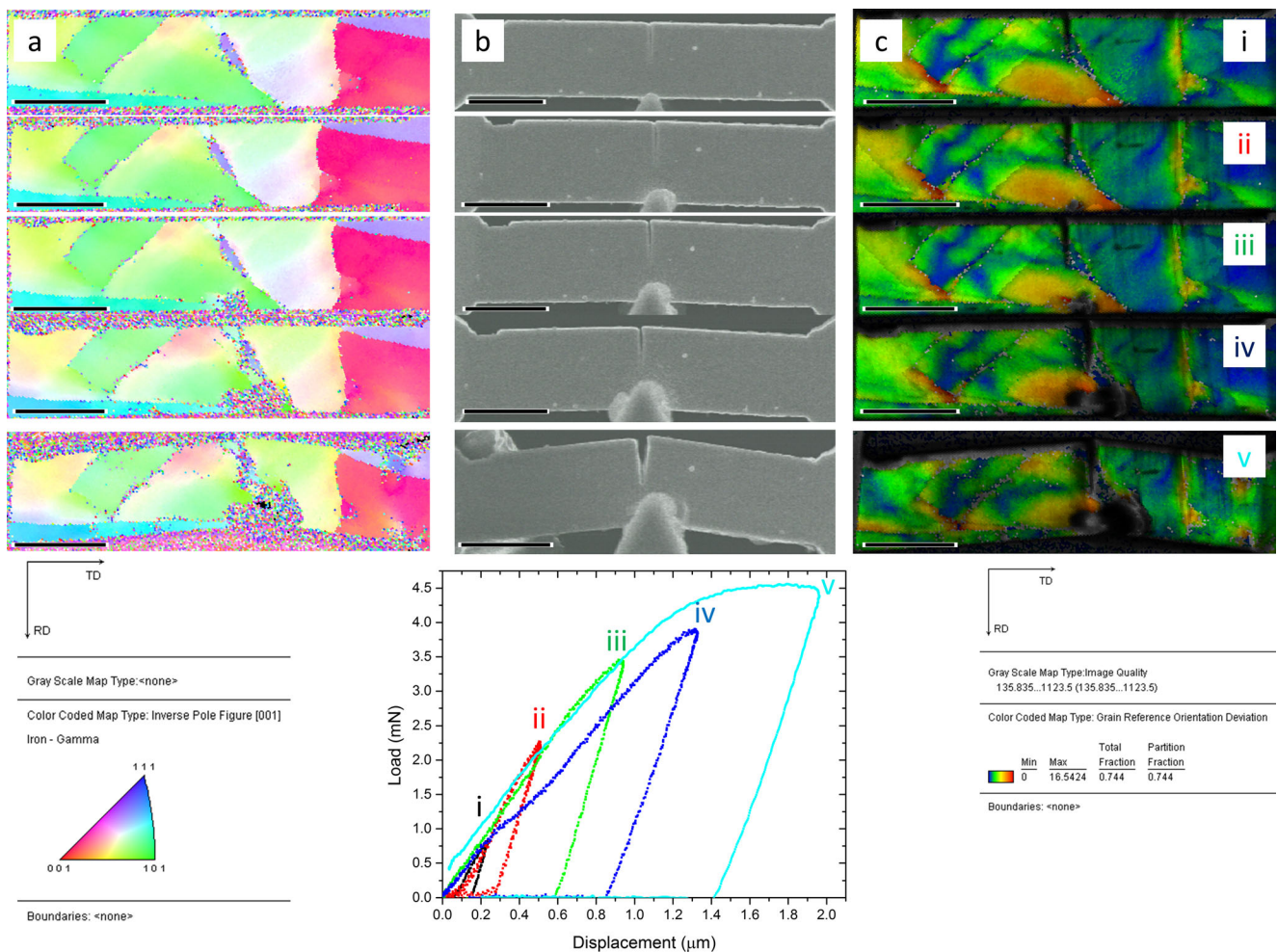


Fig. 2 An exemplary 2500 nm notched beam during stepwise loading: (a) Inverse pole figure map and corresponding color code. (b) *In-situ* SEM frames at maximum cycle load and recorded load displacement data. (c) Local misorientation map relative to the grain average orientation. The scale bar is 5 μm long. *i-v* indicates the test cycle number. Note that the *in-situ* SEM frames are at peak load, while the EBSD data are taken after unloading

beams and the larger specimens. For instance, all 100 nm beams tested were single crystalline, which arose naturally due to the 10 μm grain size. Additionally, it should be noted that the sharpness of the indenter tip relative to the size of the bending beam is greatly reduced for these specimens, resulting in a reduced indentation from the indenter into the specimen. The predominant contrast feature observed as deformation occurs is related to strain or bending contours in and out of the viewing plane. In addition to the bend contours, there is a dark region that develops directly underneath the indenter tip, which is retained upon unloading, shown in more detail in Fig. 4 *ii*e and *iii*e. This could be related to a higher dislocation density, such that this dark region corresponds to the plastic zone in front of the crack tip. The load–displacement data shows expected highly ductile behavior, but in the plastic regime, the load slightly decreases in a steady manner with each testing cycle. This may be attributable to the formation of secondary cracks on the compressive side of the bending beam near the clamped ends, where a stress concentration

from the clamping constraint exists. The sudden rise in load after cycle *vi* is attributed to the indenter running out of clearance and making additional side contact.

Theoretical Procedures

In order to determine applied stress intensities, a linear elastic fracture mechanics method (LEFM) for 3-point bending is applied. An LEFM method by Bakker [35] allows larger a/W ratios up to 0.95 as compared to the ASTM E 399 standard for 3-point bending. From the tabulation of $f_k(\alpha)$ for various values of $\alpha = a/W$ and crack lengths the stress intensity can be determined from:

$$K_1 = \sigma_b \left[\frac{(1 + \alpha)}{(1 + \alpha^2)} \right] \sqrt{\pi a} \quad (1)$$

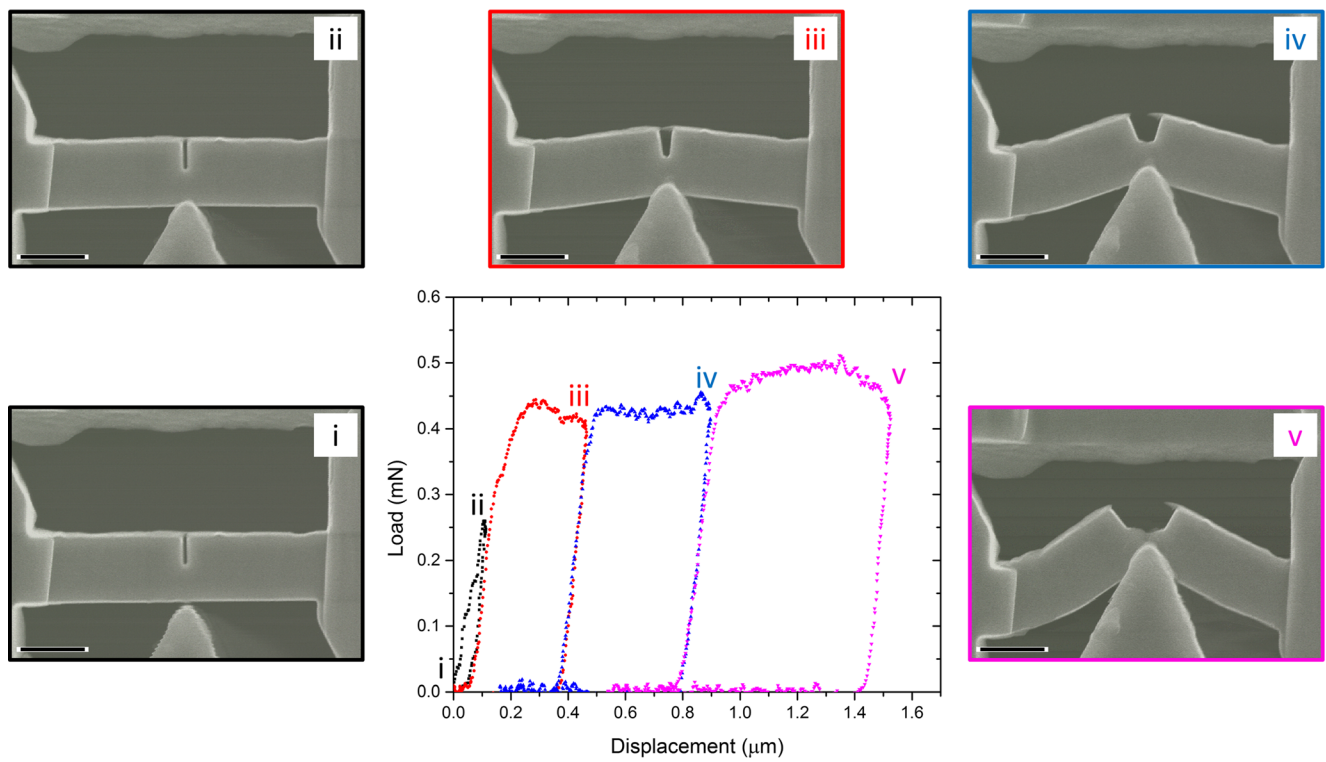


Fig. 3 *In-Situ* SEM images and corresponding Load–displacement data for a 500 nm beam with indication for the location of SEM video frames *i-v*. Scale bar is 1 μm

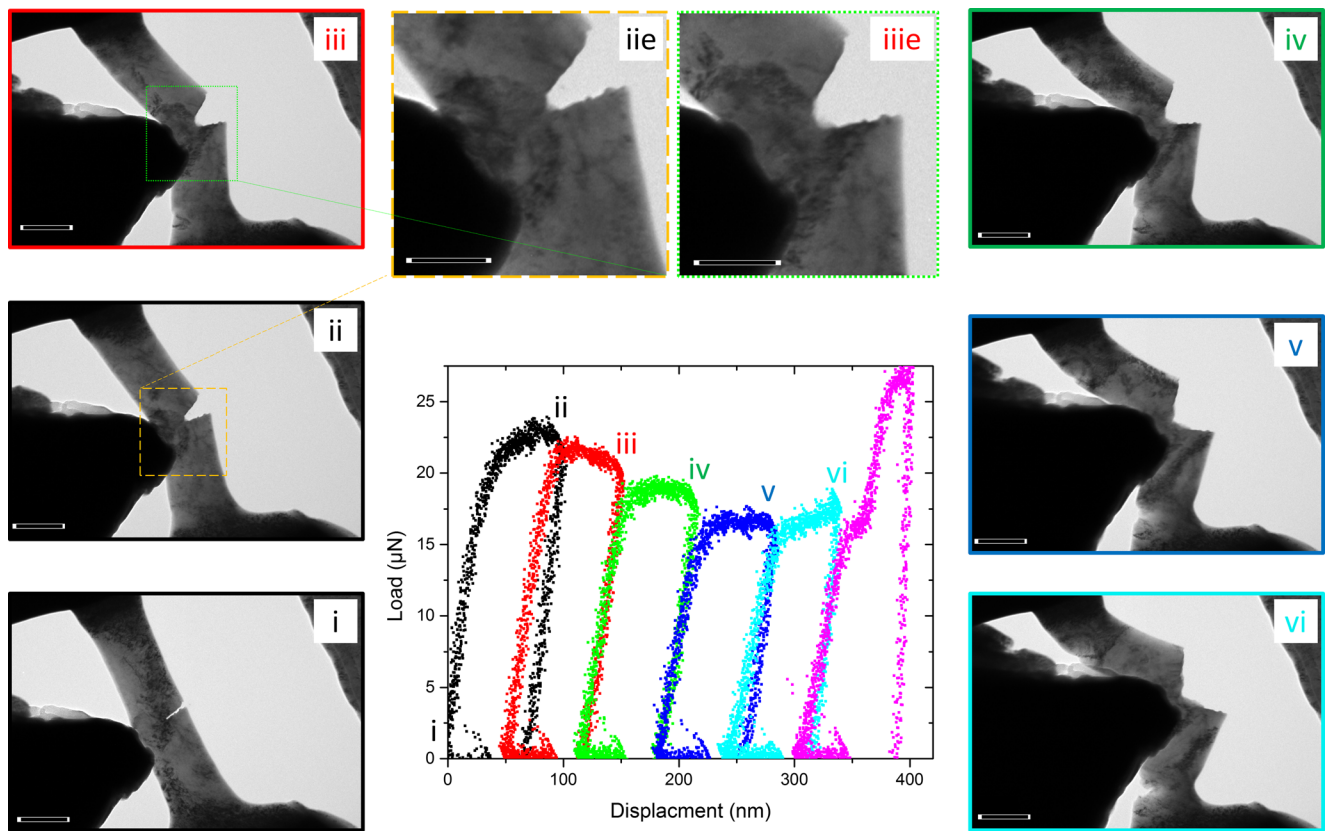


Fig. 4 Load–displacement data for a 100 nm beam with indicated positions of frames *i-vi* from the *in-situ* TEM video. Two enhanced magnification images (noted by a hatched box and an e) show evidence of a plastic zone directly under the notch root. Scale bar is 200 nm in all images

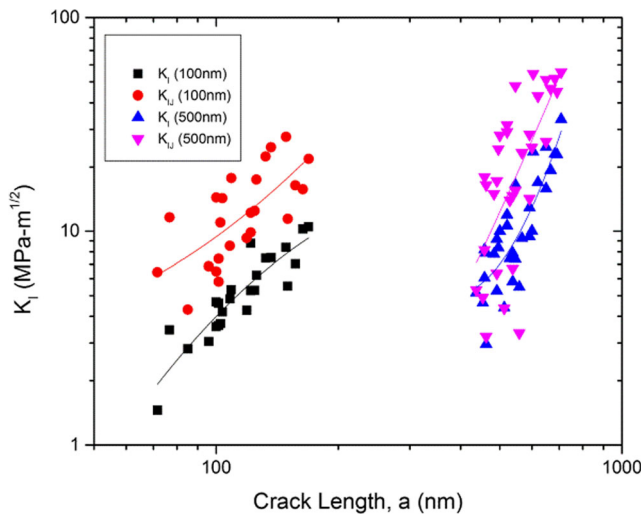


Fig. 5 Stress intensity factor vs. crack length a for 100 nm and 500 nm beams, with both K_I calculated by equation (3) and K_{IJ} calculated by equation (4), respectively

where σ_b is $(PL)/(BW^{3/2})$, where P is the load, L is the span, B is the thickness, W is the width, and $f_k(\alpha)$ is:

$$f_k(a) = \frac{1.0731 - \alpha(1 - \alpha)(1.1980 - 5.1240\alpha + 7.3327\alpha^3 - 3.1403\alpha^2)}{1 + 1.8706\alpha} \tag{2}$$

We also utilized a J-Integral approach to account for plasticity occurring during the fracture process. The result for deep cracks was again given by Bakker [35]:

$$J_I = \left[\frac{(1 + \alpha_0)}{(1 + \alpha_0^2)} \right] \frac{2A_{total}}{Bb} \tag{3}$$

where b is the remaining ligament in front of the crack, A_{total} is the total area under the load–displacement curve, B is the beam thickness and α_0 is given by:

$$\alpha_0 = 2\sqrt{\left[\left(\frac{a}{b}\right)^2 + \left(\frac{a}{b}\right) + \frac{1}{2} \right] - 2\left(\frac{a}{b} + \frac{1}{2}\right)} \tag{4}$$

The analysis methods in equations (1–4) are over-simplified. There are several complicating factors when considering analysis of these specimens, which are discussed in detail in Appendix A3. A brief summary of these issues are outlined:

1. As the crack advances towards the compressive surface, K_I rapidly increases.
2. The stress field from the indenter stabilizes the crack advance by applying a strong localized stress field, but for a

sharp tip (relative to the size of the specimen) this stress field is complex and possesses a strong gradient.

3. Similar to 2, the tip can indent the specimen, such that the ligament is being reduced from two directions, via crack advance and plastic flow under the indenter.
4. Unaccounted for plastic energy dissipation is occurring at the clamping constraints.

These issues could largely be resolved by utilizing two important revisions. First, a flat tip simulating a four point bending test would simplify the stress field from the indenter and reduce indentation of the tip into the specimen, alleviating 2&3. Secondly, finite element analysis would account for 1&4, especially one which incorporates a stress–strain law determined by supporting pillar compression experiments, such as the analysis method proposed by Shih [36].

Analysis

Using the theoretical procedures described in equations (1–4), the K_I and K_{IJ} values were determined for all tested 100 nm and 500 nm beams, as plotted versus crack length a in Fig. 5. It is observed that the values of K_{IJ} are significantly higher than for K_I , as expected due to the ductile nature of the material being studied. It should be emphasized that all these values represent a lower bound estimate of K_C , as the crack does not achieve an unstable opening displacement and thus is not in the critical state. Instead of failure by critical crack instability, it appears that crack advance takes place through a ductile tearing process. In Appendix A4, comparisons between stress intensities calculated in equation (3) versus a crack tip opening displacement method were performed and

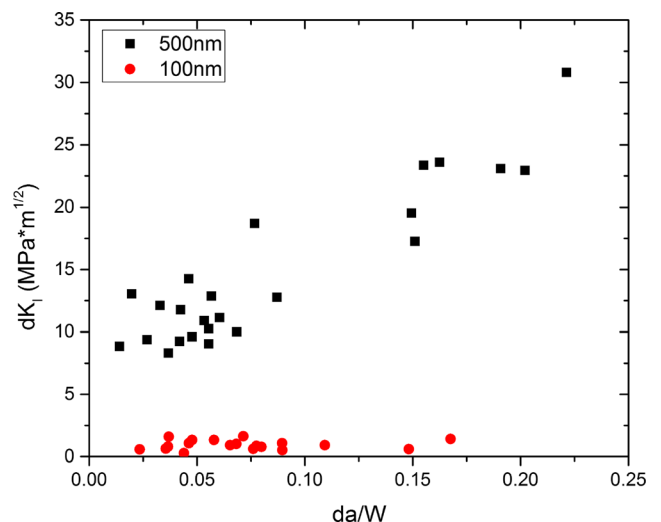
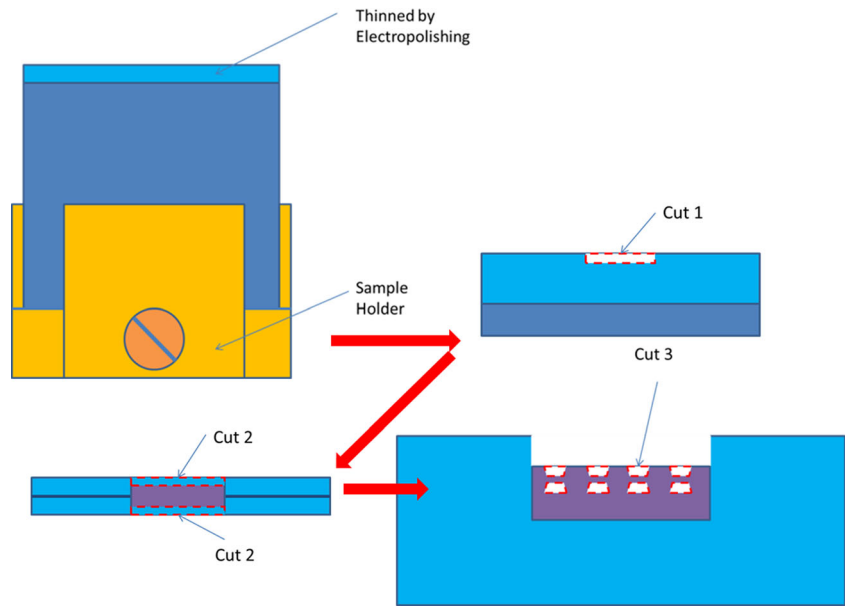


Fig. 6 dK_I vs. da/W for 100 and 500 nm beams; da is normalized by the beam width for comparison of the different sizes

Fig. 7 Schematic showing the multistep process to fabricate testing specimens indicated as Cuts 1–3



found to agree, which suggests equation (3) is valid, but the issues (1–4) outlined in the theoretical methods section must be kept in mind.

Evans and Suo [37] demonstrated and verified that the strain energy release rate for channel cracking was proportional to the film thickness, such that $G_I \sim \sigma_{ys}^2 h/E$. In our case, the resistance does appear to shift to higher values with increasing thickness in Fig. 5. As can be seen from equation (3), the only difference in K_I emerges from the term $a^{1/2}$ if a/W is kept constant. In LEFM then, one might expect K_I to be about $5^{1/2}$ larger for the thicker 500 nm beam, which is consistent with our experimental observations. However, the steepness in dK_I vs. da is more pronounced for the thick beam than the

thinner one. This is shown in detail Fig. 6, where dK_I vs. da/W (a is normalized by W for comparison purposes) is approximately flat for the 100 nm beam, but increasing with a rate of 0.11 MPa-m^{1/2}/nm for the 500 nm beams. It is difficult to compare these measurements directly to other literature, given how thin the specimens here are, but these values seem reasonable for a plastic tearing process in a high toughness material. As previously discussed, Paviot and Vlassak [20] found stress intensity values for thin film crack growth for Au (0.45 MPa-m^{1/2}) and Al (0.515 MPa-m^{1/2}), which is an order of magnitude less than what is measured here. This is reasonable, since they studied pure materials while Nitronic 50 possesses significant alloying.

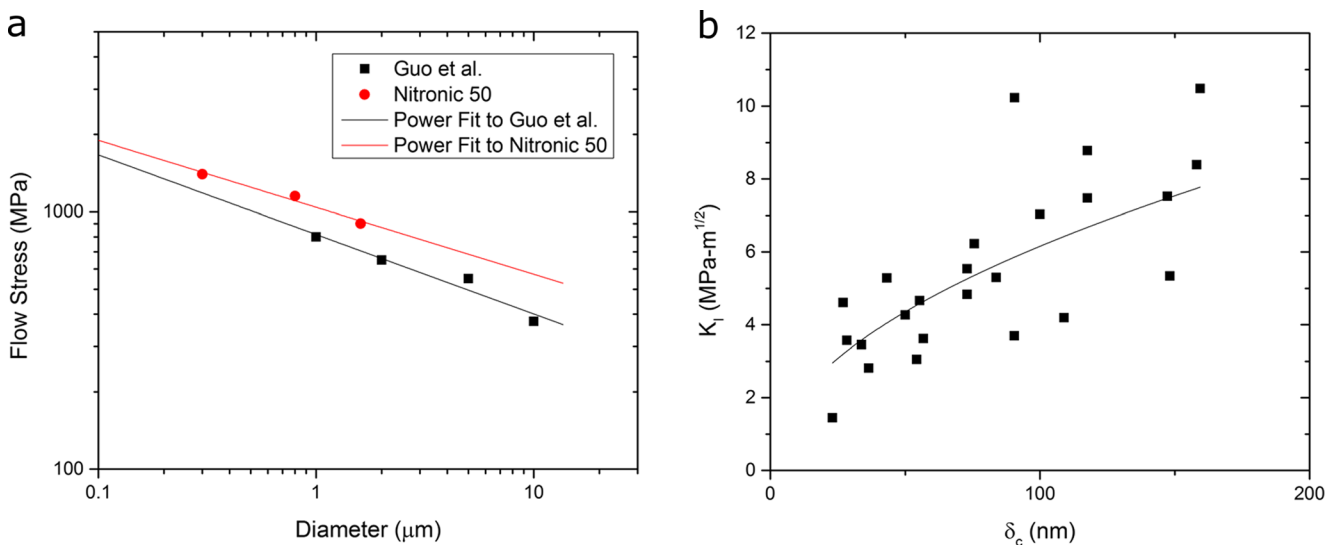


Fig. 8 (a) Flow stress vs. size from micropillar compression data on Nitronic 50 extrapolated to 100 nm (b) Stress intensity values derived from equation (3) versus the measured crack opening displacement (points) and the prediction from equation (A.5) (line) for 100 nm beams

Conclusions

In-situ doubly-clamped bending beam experiments were performed *in-situ* in the SEM and TEM, respectively. This testing scheme was demonstrated to give high visibility of the crack tip behavior and stability of the crack front, allowing the use of further characterization techniques. This is demonstrated by EBSD scanning between deformation cycles, which showed measureable changes in the grain orientations and evolution of the local misorientation ahead of the crack tip. Drastic improvements in notch sharpness were also achieved using an electron beam notching approach. Several improvements were also recommended, including use of a flat tip to simulate four point bending and by using finite element approaches with the support of an elastic–plastic law derived from pillar compression on a similar scale. Despite this, analysis showed a reasonable scaling for applied stress intensities with size based upon available plastic dissipation volume.

Acknowledgments Funding by INL (DOE) Grant #00109759 (Subcontract to DE-AC07-951014517) and the Marshall Plan scholarship foundation via Montanuniversität Leoben. The authors would also like to thank Ruth Treml, Peter Imrich and Stefan Wurster for their help on this project. DK acknowledges funding from the Austrian Science Fund FWF (project number P25325-N20).

A1) Fabrication Details

FIB milling of a prepared lamellae was accomplished using a Zeiss LEO1540XB operating at 30 keV by multiple steps shown schematically in Fig. 7. First, the rounded electropolished edge was cut flat using a large beam current of 10 nA from the side, shown as Cut 1. The sample was then turned, reinserted into the FIB, and milled on both sides to produce lamellae of thickness appropriate for the size of samples being fabricated, typically 3× thicker than the final bending beam geometry, utilizing 10 nA current, indicated by Cut 2. At this point, the beam current was reduced to 0.5 nA to create the basic shape of the bending beams by removing material above and below the beam, see Cut 3. Next, careful reduction in size to the final dimension, smoothing the sides and removing FIB tapering was achieved by multiple cuts. This required reinsertion into the instrument to cut from both the top and from the sides. These final cuts were accomplished by using a beam current of 50pA and tilting by 2° into the side walls of the bending beam.

A2) Notch Radius

One issue that requires some attention is whether the pre-notches realistically replicate a sharp crack. Focusing of the ion or electron beam used to produce the notches in this study

is imperfect and results in a significant radius of curvature at the root of the notch. One way of viewing the problem was developed by Drory et al. [38] and is presented as equation (A.1):

$$K'_{Ic} = \left(1 + \frac{\rho}{2x}\right)K_{Ic} \quad (\text{A.1})$$

where the effective stress intensity factor K'_{Ic} is modified from the ideal K_{Ic} . The ratio of the radius of curvature, ρ , to a somewhat ambiguous length scale factor, x , determines the magnitude of this effect. This was later refined by Pugno et al. [39] and applied by Armstrong et al. to *in-situ* fracture testing [40], by introducing an asymptotic correction, which is presented as equation (A.2):

$$K'_{Ic} = \sqrt{1 + \frac{\rho}{2d_0}}K_{Ic} \quad (\text{A.2})$$

where d_0 is given by equation. (A.3)

$$d_0 = \frac{2}{\pi} \frac{K_{Ic}^2}{\sigma_u^2} \quad (\text{A.3})$$

where σ_u is the ultimate strength of the material. Considering the FIB notched 500 nm and 2500 nm bending beams, reasonable values to use are an ultimate strength of 1 GPa measured previously from pillars of Nitronic 50 of a similar size (1.5 μm diameter), a rough average measured value for K_I of 10 $\text{MPa}\cdot\text{m}^{1/2}$, and a generous value for the radius of curvature of 100 nm, one gets a correction factor of 1.00039. Clearly this correction is of minor concern for such a notch in a ductile material. One should keep in mind that these concepts were initially developed for macroscopic samples and cracks, therefore they might have limitations when applied to miniaturized samples.

A3) Concerns

There are a number of currently unaddressed issues with this experimental design. First, these deeply cracked bend beams experience a rapidly increasing K_I as the crack approaches the back free surface. Second, the support of the nanoindenter on the compressive side, while giving good stability to the system as previously discussed by Jaya et al. [25–27], does represent a contact stress gradient. This introduces added complexity to the stress analysis, as the plastic zone from the indentation will interact with the plastic zone at the root of the notch, as described by Chen and Bull [41]. An indentation stress calculation demonstrated a substantially smaller stress from a plasticity standpoint. Using the contact cross-section to estimate the contact flow stress based upon load and imaged contact area,

this was determined to be about half of the bending stress. Notably, the situation improves for smaller beams, where the reduced bending loads limit the penetration depth (Fig. 4). Additionally, clamping of the beam is a necessary feature, but this results in mechanical work being dissipated into the clamped region that is not correctly accounted for in the applied J-integral method. Given these challenges, it is clear that the use of Finite Element (FE) or other advanced computational methods will allow to more accurately determine applied stress intensity values.

Secondly, the LEFM or J-integral approach may not be the best descriptor for these very small beams. Earlier studies [42] raised questions about whether or not LEFM or LEFM-based J-integral analysis was always correct. Atluri, et al. [43] showed that a T^* criteria may be more appropriate for the complete unloading and reloading format of Figs. 4, 5 and 6. Their concern was that the path-independent integral, J , could be quite different if the plastic zone was elongated to include plasticity in the crack wake, rather than just the plasticity at the front of the crack. In one of the 100 nm beams there was an indication of dislocations in the crack wake, shown in Fig. 4 iiiie, where a dark contrast feature is seen along the notch flank. As this is a bright field image, this is still an open question and not a certain proof. However, it is clear in Fig. 4 that substantial dislocation plasticity was generated during the crack growth process. These observations for the first two load and re-load curves shown in Fig. 4 represent K_I values according to equation (3) of 3.2 and 4.2 MPa-m^{1/2}. Using a first-order estimate of the plastic zone diameter of $\pi(K_I/\sigma_{ys})^2$, one evaluates plastic zone sizes at least a factor of four larger than those observed in Fig. 4. It is apparent that additional numerical approaches are required to address plasticity-based slow crack growth in such small-scale bend beams. Previously, we have shown that smaller is tougher for compression of brittle materials that are small in two or three dimensions [14].

The J-integral approach utilized here from equation (4) is standard; a possible refinement would consider the local plastic deformation at the root of the crack and the corresponding local yield stress specifically [44].

A4) Using CTOD as a Verification Technique

In order to determine the viability of the analysis in equations (3–5), they were compared against applied stress intensity factors calculated by crack tip opening displacement [45], δ_c , which is given for plane stress as:

$$\delta_c = \frac{K_I^2}{\sigma_{ys}E} \quad (\text{A.5})$$

where K_I is the opening mode applied stress intensity, σ_{ys} is the yield strength and E is the modulus of elasticity. Given that

flow stress is enhanced with reduced dimensions, estimation of a reasonable yield stress to use in conjunction with equation (1) required extrapolation of previous data. The yield strength was extrapolated from FIBed nano-pillar compression data for Nitronic 50 and from the austenitic phase of a duplex steel [46]. The data are shown in Fig. 8(a) for a range of pillar diameters ranging from 300 nm to 10 μm . The extrapolation to 100 nm gave a flow stress of approximately 1900 MPa.

Values of δ_c were measured directly from the video using the standard 90° intercept method. Values of K_I calculated by equation (3) were plotted against measured δ_c values as shown in Fig. 8(b), with the extrapolated flow stress of 1900 MPa inserted into equation (1) to produce the overlaying fitting line. This shows that there is good agreement between analysis using equations (1) and (3) for beams of 100 nm thickness, partially validating the analysis presented. Notably, this analysis assumes no strain hardening, which appears reasonable as repeated loading exhibits little hardening, as one would expect since the 100 nm section thickness allows easy dislocation termination at surfaces.

References

1. De Wolf I, Van Spengen WM (2002) Techniques to study the reliability of metal RF MEMS capacitive switches. *Microelectron Reliab* 42(9–11):1789–1794
2. Lee H, Coutu RA, Mall S, Leedy KD (2006) Characterization of metal and metal alloy films as contact materials in MEMS switches. *J Micromech Microeng* 16(3):557
3. Lacour SP, Jones J, Suo Z, Wagner S (2004) Design and performance of thin metal film interconnects for skin-like electronic circuits. *Electron Device Lett IEEE* 25(4):179–181
4. Faupel F, Yang CH, Chen ST, Ho PS (1989) Adhesion and deformation of metal/polyimide layered structures. *J Appl Phys* 65(5):1911–1917
5. Wellner P, Kraft O, Dehm G, Andersons J, Arzt E (2004) Channel cracking of β -NiAl thin films on Si substrates. *Acta Mater* 52(8):2325–2336
6. Cordill MJ, Taylor A, Schalko J, Dehm G (2010) Fracture and delamination of chromium thin films on polymer substrates. *Metall Mater Trans A* 41(4):870–875
7. Read DT, Dally JW (1995) Fatigue of microlithographically-patterned free-standing aluminum thin film under axial stresses. *J Electron Packag* 117(1):1–6
8. Kodaera M et al (2005) Stress corrosion cracking of Cu interconnects during CMP with a Cu/porous low-k structure. *J Electrochem Soc* 152(6):G506–G510
9. Volinsky AA, Vella JB, Gerberich WW (2003) Fracture toughness, adhesion and mechanical properties of low- K dielectric thin films measured by nanoindentation. *Thin Solid Films* 429(1):201–210
10. Kim K, Artyukhov VI, Regan W, Liu Y, Crommie MF, Yakobson BI, Zettl A (2011) Ripping graphene: preferred directions. *Nano Lett* 12(1):293–297
11. Sundararajan S, Bhushan B (2002) Development of AFM-based techniques to measure mechanical properties of nanoscale structures. *Sensors Actuators A Phys* 101(3):338–351

12. Ast J, Przybilla T, Maier V, Durst K, Göken M (2014) Microcantilever bending experiments in NiAl—Evaluation, size effects, and crack tip plasticity. *J Mater Res* 29(18):2129–2140
13. Völker B, Venkatesan S, Heinz W, Matoy K, Roth R, Batke JM, Roth R, Batke J-M, Cordill MJ, Dehm G (2015) Following crack path selection in multilayer structures with weak and strong interfaces by *in situ* 4-point-bending. *J Mater Res* 30(08):1090–1097
14. Beaber AR, Nowak JD, Ugurlu O, Mook WM, Girshick SL, Ballarini R, Gerberich WW (2011) Smaller is tougher. *Philos Mag* 91(7–9):1179–1189
15. Krafft JM, Sullivan AM, Boyle RW (1961) Effect of dimensions on fast fracture instability of notched sheets. *Proc Crack Propag Symp* 1:8–28
16. Brown WF, Srawley JE (1966) Plane strain crack toughness testing of high strength metallic materials. ASTM International, Philadelphia
17. Knott JF (1973) Fundamentals of fracture mechanics. Gruppo Italiano Frattura
18. Hellan K (1984) Introduction to fracture mechanics. McGraw-Hill, New York
19. Hosokawa H, Desai AV, Haque MA (2008) Plane stress fracture toughness of freestanding nanoscale thin films. *Thin Solid Films* 516(18):6444–6447
20. Paviot VM, Vlassak JJ, Nix WD (1994) Measuring the mechanical properties of thin metal films by means of bulge testing of micromachined windows. *MRS Proc* 356:579, Cambridge University Press
21. Chen J, Bull SJ (2006) Assessment of the toughness of thin coatings using nanoindentation under displacement control. *Thin Solid Films* 494:1–7
22. Haque MA, Saif MTA (2002) In-situ tensile testing of nano-scale specimens in SEM and TEM. *Exp Mech* 42(1):123–128
23. Dehm G, Legros M, Heiland B (2006) In-situ TEM straining experiments of Al films on polyimide using a novel FIB design for specimen preparation. *J Mater Sci* 41(14):4484–4489
24. Minor AM, Asif SS, Shan Z, Stach EA, Cyranowski E, Wyrubek TJ, Warren OL (2006) A new view of the onset of plasticity during the nanoindentation of aluminium. *Nat Mater* 5(9):697–702
25. Jaya BN, Jayaram V, Biswas SK (2012) A new method for fracture toughness determination of graded (Pt, Ni) Al bond coats by micro-beam bend tests. *Philos Mag* 92(25–27):3326–3345
26. Jaya BN, Jayaram V (2014) Crack stability in edge-notched clamped beam specimens: modeling and experiments. *Int J Fract* 188(2):213–228
27. Jaya BN, Kirchlechner C, Dehm G (2015) Can microscale fracture tests provide reliable fracture toughness values? A case study in silicon. *J Mater Res* 30(05):686–698
28. Moser G, Felber H, Rashkova B, Imrich PJ, Kirchlechner C, Grosinger W, Motz C, Dehm G, Kiener D (2012) Sample preparation by metallography and focused ion beam for nanomechanical testing. *Pract Metallogr* 49(6):343–355
29. Egerton RF, Cheng SC (1987) Measurement of local thickness by electron energy-loss spectroscopy. *Ultramicroscopy* 21(3):231–244
30. Kumar S, Li X, Haque MA, Gao H (2011) Is stress concentration relevant for nanocrystalline metals? *Nano Lett* 11(6):2510–2516
31. Kumar S, Haque MA, Gao H (2013) Transformation induced toughening and flaw tolerance in pure nanocrystalline aluminum. *Int J Plast* 44:121–128
32. Kiener D, Zhang Z, Sturm S, Carzottes S, Imrich PJ, Kirchlechner C, Dehm G (2012) Advanced nanomechanics in the TEM: effects of thermal annealing on FIB prepared Cu samples. *Philos Mag* 92(25–27):3269–3289
33. May J, Höppel HW, Göken M (2005) Strain rate sensitivity of ultrafine-grained aluminium processed by severe plastic deformation. *Scr Mater* 53(2):189–194
34. Schwarzer RA (1997) Advances in crystal orientation mapping with the SEM and TEM. *Ultramicroscopy* 67(1):19–24
35. Bakker AD (1995) Evaluation of elastic fracture mechanics parameters for bend specimens. *Int J Fract* 71(4):323–343
36. Shih CF (1981) Relationships between the *J*-integral and the crack opening displacement for stationary and extending cracks. *J Mech Phys Solids* 29(4):305–326
37. Ye T, Suo Z, Evans AG (1992) Thin film cracking and the roles of substrate and interface. *Int J Solids Struct* 29(21):2639–2648
38. Drory MD, Dauskardt RH, Kant A, Ritchie RO (1995) Fracture of synthetic diamond. *J Appl Phys* 78(5):3083–3088
39. Pugno N (2005) Predictions of strength in MEMS components with defects - a novel experimental–theoretical approach. *Int J Solids Struct* 42(2):647–61
40. Armstrong DEJ, Haseeb ASMA, Roberts SG, Wilkinson AJ, Bade K (2012) Nanoindentation and micro-mechanical fracture toughness of electrodeposited nanocrystalline Ni–W alloy films. *Thin Solid Films* 520(13):4369–4372
41. Chen J, Bull SJ (2013) Finite element modelling of delamination in multilayer coatings. *Nanosci Nanotechnol Lett* 5(7):795–800
42. Alturi SN, Nishioka TL, Nakagaki M (1984) Incremental path-independent integrals in inelastic and dynamic fracture mechanics. *Eng Fract Mech* 20(2):209–244
43. Brust FW, McGowan JJ, Atluri SN (1986) A combined numerical/experimental study of ductile crack growth after a large unloading using T^* , J and CTOA criteria. *Eng Fract Mech* 23(3):537–550
44. Chen J, Bull SJ (2006) On the relationship between plastic zone radius and maximum depth during nanoindentation. *Surf Coat Technol* 201(7):4289–4293
45. Zhu X-K, Joyce JA (2012) Review of fracture toughness (G , K , J , CTOD, CTOA) testing and standardization. *Eng Fract Mech* 85:1–46
46. Guo EY, Xie HX, Singh SS, Kirubanandham A, Jing T, Chawla N (2014) Mechanical characterization of microconstituents in a cast duplex stainless steel by Micropillar compression. *Mater Sci Eng A* 598:98–105